Supporting Information

Jao *et al.* 10.1073/pnas.0807826105

SI Methods

Structural Refinement. ***Structure building.*** A peptide of the sequence shown in supporting information (SI) Fig. S5 (where X = label) was built by using an in-house algorithm. The peptide was constructed as a linear α-helix ($\phi = -57.0°$, $\psi = -47.0°$, $\omega = 180.0°$, $\chi 1$ (C^{γ}–C^{β}–C^{α}–N) = 168.0°) with the center of the helical axis (at V49) positioned 146 Å from the center of an imaginary spherical lipid vesicle whose outer diameter is ≈300 Å (Fig. S5). Twenty-six labels were added with torsion angles $t1$ (S^{γ}–C^{β}–C^{α}–N) = −60° and $t2$ (S^{δ}–S^{γ}–C^{β}–C^{α}) = −60°, because these angles are favorable for the label bound to an α-helix (1).

Simulated annealing molecular dynamics (SAMD) calculations. Experimental data for 12 interlabel distances (11R1/26R1, 11R1/41R1, 22R1/52R1, 26R1/56R1, 37R1/67R1, 41R1/56R1, 41R1/67R1, 41R1/70R1, 44R1/67R1, 48R1/67R1, 56R1/86R1, 63R1/81R1) and 25 label "depths" (Table S1) were used to define restraints for the SAMD calculations. These data were converted into an appropriate format for use as restraints in AMBER8. The allowable ranges used for the interlabel distances and the depths (Table S2) were established through a series of preliminary SAMD calculations in which these ranges were varied. Similarly, restraints were defined for geometrical elements of the α-helix (Table S2). We also included a restraint for the H^{α}–S^{δ} distance in each label, because it has been established that an interaction persists between these atoms and reduces the mobility of the label (1–4). No other restraints were applied to the label. Parameters for the label backbone and side chain up to S^{δ} were identical to those used in AMBER8 for a S–S cysteine–cysteine bridge. The parameters for the remainder of the label were based on those reported for a similar label bound to DNA (5).

The SAMD calculations were carried out in AMBER8. Lysine and glutamic acid residues were included in uncharged forms: residues KNC and ENC in the AMBER parm98 force field. These residues contain NH_3 and COO groups on the respective side chains, but the overall charge on each residue is neutral. Preliminary calculations indicated that inclusion of charged residues in gas phase SAMD calculations resulted in formation of salt bridges between adjacent lysine and glutamic acid side chains. This is not likely to occur in an aqueous or interfacial environment, and therefore we chose to use the uncharged residues in the final calculation.

After a brief minimization of the starting structure (Fig. S5) SAMD was performed in cycles of 30 ps, including a heating phase from 0 to 1,200 K in 4 ps using a step of 0.002 ps, during which the force constants for the restraints were increased from 0.1 to 10.0; maintenance of the temperature at 1,200 K for a further 6 ps; and then cooling to 0 K over 20 ps, with stepwise adjustments of the TAUTP parameter. This approach was based on the standard recommended protocol for simulated annealing calculations in the AMBER8 manual (6) with some minor modifications. Eleven cycles were performed, including an initial equilibration cycle, and 10 subsequent production cycles (numbered 1 to 10) from which structures were collected at 0 K. The molecular dynamics simulation was performed with a time step of 0.002 ps, a distance-dependent dielectric of 4, and a cut-off of 10.0 Å. The "atom" representing the center of the imaginary lipid vesicle was constrained to the origin with a force constant of 1000.0 kcal·mol^{-1}·Å^{-1}. Full details of the parameters and input files used to perform the SAMD calculations will be provided upon request.

Because calculations using EPR data to refine a structure by using simulated annealing have not been reported previously, some clarification of the method is required. First, the molecule used in the calculation was the peptide with labels substituted at all positions for which interlabel distance or depth data were used. Interlabel distances were defined between the N atom of the nitroxide groups of each label pair. The only other element in the calculation was an "atom" representing the center of an imaginary vesicle. This "atom" was used to define the "depth" of the peptide in the lipid bilayer via distance restraints from the N of the nitroxide to the center atom. As seen in *Results*, this procedure caused the peptide to bend in a manner consistent with its insertion into the lipid outer leaflet. It should be noted that the present computational treatment of the experimentally obtained immersion depths is based on the assumption that α-synuclein does not cause significant local alterations in membrane shape. Although some proteins can affect the curvature of larger vesicles (7, 8), α-synuclein does not appear to have this ability; rather α-synuclein binds preferentially to curved vesicles (9) without disrupting the integrity of the POPS/POPC-containing vesicles used here (Fig. S4*D*). More importantly, the present studies were performed using SUVs. Such vesicles have an extreme curvature strain, and even curvature-inducing proteins are not known to generate smaller, more highly curved vesicles. We therefore reason that substantial deformation of SUVs would further enhance the curvature strain and create a significant energetic barrier. The present approach of converting depth measurements into distance restraints is likely to be applicable to other proteins, but extra caution may need to be exercised when applying this approach to proteins bound to larger vesicles. A central feature of the experimental design was that the distances were chosen to be interlocking; that is, each position was constrained by multiple inter-residue distances, as well as the distance to the vesicle center. This strategy was chosen to counteract the intrinsic flexibility of the nitroxide side chain.

Validation of results. A family of 10 synuclein structures was obtained from the SAMD calculations. To validate the results, we examined how well these structures reproduced experimental data that were not included in the constraints. In particular, the depths of K32, K34, K43, K45, K58, K60, and K80 in each structure were compared with the experimentally determined depths of these residues by calculation of a "lysine depth parameter." This parameter was calculated based on the distance of the N^{ζ} atoms to the center of the lipid vesicle, as described in the legend to Fig. S6. The parameter is shown for four points in each SAMD cycle (Fig. S6), reflecting the initial heating, rapid high-temperature heating, slow cooling, and final cooling stages, and generally the lysine depth parameters reflect the expected behavior in the simulation. For example, for cycle 1 (the first four data points in Fig. S6) the lysine depth parameter increases from the first (△) to the second (○) point, reflecting heating of the system and greater disorder causing a larger difference between the experimental and theoretical data, and then drops at the third (□) point, reflecting cooling of the system, and reaches a minimum at the end of the cycle (■).

The other cycles in Fig. S6 show behavior largely similar to that described for cycle 1, in that the second point in each cycle (○) is generally the maximum and the fourth point is the minimum (■). There is some fluctuation of the depth parameter, in part due to the assumption that the N^{ζ} atom of the lysine reflects the position of the nitroxide of a spin label at the same position. The two biggest deviations from the experimental depth measurements were obtained for cycles 4 and 7. Inspection of the structure for cycle 7 indicated that this structure has the same

fold as all other structures but that the specific lysine side chain (but not backbone) orientations were responsible for the deviation. The only other structure that did not give the expected result was that from cycle 4. This structure had the largest value for the depth parameter (Fig. S6) and was the only structure for which this value was >3 Å. Visual inspection of the structure from cycle 4 indicated that it was substantially different from all other structures. Importantly, the structure was tilted in a way that caused the lysine positions in the N-terminal region to point toward the acyl chain interior of the bilayer, an arrangement that is inconsistent with the depth data and the helical wheel in Fig. 1. Therefore, we chose to eliminate this structure from the final family of derived structures. It should be pointed out, however, that the SAMD simulations "recovered" from this structure and reverted back to giving structures that were consistent with experimental data in cycles 5–10.

We also determined the agreement between the theoretical and experimental data for two interlabel distances (26R1/41R1 and 56R1/70R1) that were not included as constraints in the SAMD calculation. The values for these distances are shown in Table S3 for the 9 structures (cycles 1–3 and 5–10). All distances are within the experimentally observed distance ranges (Table 1), and most are within 1 or 2 Å of the respective distance maxima.

The ϕ and ψ values averaged over all amino acids in each structure are also shown in Table S3 and illustrate that the majority of the angles did not approach the edges of the respective restraint ranges for ϕ and ψ (Table S2). ϕ changed from $-57°$ in the linear helical starting structure (Fig. S5) to an overall average (across all amino acids and all structures) of about $-65 \pm 4°$, whereas ψ moved from $-47°$ (Table S3) to an overall average of about $-42 \pm 7°$. Most of the individual ϕ and ψ angles were well within the constraint range.

Four-Pulse DEER Experiments. The ELDOR pump frequency was set to the maximum of the central absorption peak of the nitroxide EPR spectrum, whereas the observer frequency was set to the maximum of the low-field absorption peak. The observer pulse lengths used were 16 and 32 ns, and the optimized pump pulse length was ≈32 ns, and a 2-step phase cycle was applied to eliminate the unwanted echoes. Data were acquired for 5–12 h with a repetition rate of 500 Hz. DEERAnalysis2006 and DEERAnalysis2008 packages (10) were used to obtain distance information from the dipolar time evolution data. The background contribution from nonspecific interaction was subtracted, using a two-dimensional model for vesicle-bound α-synuclein and a three-dimensional model for SDS-bound α-synuclein. For α-synuclein bound to nonvesicular POPG the background dimensionality was fit by using DEERAnalysis2008. Tikhonov regularization was used with regularization parameters of 100 or less obtained from the L-curve analysis to fit distances (10, 11). The distances given in Table 1 correspond to the maximum in the Tikhonov distance distributions. Importantly, fits using Gaussian distance distributions (using DEFit kindly provided by Peter Fajer, Florida State University, as well as custom programs kindly provided by Christian Altenbach, University of California Los Angeles) gave distance maxima that were within 0.5 Å of those obtained from Tikhonov regularization.

Interaction with SDS Micelles. To study the interaction with SDS micelles, we adopted conditions previously used in NMR studies (12). Samples were prepared in 20 mM Hepes pH 7.4, 100 mM NaCl buffer at a protein-to-detergent molar ratio of 1:150 (final concentration of 250 μM α-synuclein and 37.5 mM SDS). For all experiments, 25% spin-labeled protein was mixed with wild-type protein before addition of SDS (63 μM spin-labeled protein and 187 μM wild-type protein) to minimize intermolecular spin–spin interactions. Sucrose was present at 30% as cryoprotectant for flash freezing.

Dye Leakage Assays. SUVs composed of 30% POPS/70% POPC and 100% POPG loaded with 9 mM ANTS (8-aminonaphthalene-1,3,6-trisulfonic acid, disodium salt) and 25 mM DPX [*p*-xylene-bis(pyridinium bromide)] (Invitrogen) were used in the dye leakage assay. SUVs were made by first drying down lipids, then resuspending them in the ANTS/DPX solution. The resuspended lipid solution was treated to 5 cycles of freeze/thaw, then bath-sonicated for 20 min. Unencapsulated dye was removed by gel filtration using Sephadex G-100 media (GE Healthcare). Assays were performed using a 1:250 molar ratio of protein to lipid. Fluorescence measurements were made using a JASCO fluorometer (FP-6500), setting excitation at 380 nm. Emitted fluorescence was monitored at 520 nm. Experiments with 30% POPS were conducted using 20 mM Hepes (pH 7.4), 100 mM NaCl buffer, whereas those using 100% POPG were performed using 10 mM Tris (pH 7.4) to match the conditions of the prior study (13).

Gel Filtration. The thiol-reactive probe *N*,*N*′-dimethyl-*N*-(iodoacetyl)-*N*′-(7-nitrobenz-2-oxa-1,3-diazol-4-yl)ethylenediamine (IANBD amide from Invitrogen) was used to label a C-terminal single-cysteine mutant. SUVs composed of 30% POPS/70% POPC or 100% POPG were made with 0.1% rhodamine-labeled phosphatidylethanolamine. After desiccation, lipids were resuspended in 20 mM Hepes (pH 7.4), 100 mM NaCl for assays with 30% POPS/70% POPC, or 10 mM Tris (pH 7.4) for assays with 100% POPG. Protein and lipid were incubated at 1:250 molar ratio for 30 min before separation using a Superdex 200 (GE Healthcare) gel filtration column. Protein elution was monitored at 470 nm, while lipid elution was detected at 570 nm.

1. Guo Z, Cascio D, Hideg K, Hubbell WL (2008) Structural determinants of nitroxide motion in spin-labeled proteins: solvent-exposed sites in helix B of T4 lysozyme. *Protein Sci* 17:228–239.
2. Guo Z, Cascio D, Hideg K, Kalai T, Hubbell WL (2007) Structural determinants of nitroxide motion in spin-labeled proteins: Tertiary contact and solvent-inaccessible sites in helix G of T4 lysozyme. *Protein Sci* 16:1069–1086.
3. Langen R, Oh KJ, Cascio D, Hubbell WL (2000) Crystal structures of spin labeled T4 lysozyme mutants: Implications for the interpretation of EPR spectra in terms of structure. *Biochemistry* 39:8396–8405.
4. Mchaourab HS, Lietzow MA, Hideg K, Hubbell WL (1996) Motion of spin-labeled side chains in T4 lysozyme. Correlation with protein structure and dynamics. *Biochemistry* 35:7692–7704.
5. Price EA, Sutch BT, Cai Q, Qin PZ, Haworth IS (2007) Computation of nitroxide-nitroxide distances in spin-labeled DNA duplexes. *Biopolymers* 87:40–50.
6. Case DA, *et al.* (2004) *AMBER* 8 (University of California, San Francisco).
7. Gallop JL, *et al.* (2006) Mechanism of endophilin N-BAR domain-mediated membrane curvature. *EMBO J* 25:2898–2910.
8. McMahon HT, Gallop JL (2005) Membrane curvature and mechanisms of dynamic cell membrane remodelling. *Nature* 438:590–596.
9. Davidson WS, Jonas A, Clayton DF, George JM (1998) Stabilization of alpha-synuclein secondary structure upon binding to synthetic membranes. *J Biol Chem* 273:9443–9449.
10. Jeschke G, *et al.* (2006) DeerAnalysis2006—a comprehensive software package for analyzing pulsed ELDOR data. *Appl Magn Reson* 30:473–498.
11. Chiang YW, Borbat PP, Freed JH (2005) The determination of pair distance distributions by pulsed ESR using Tikhonov regularization. *J Magn Reson* 172:279–295.
12. Ulmer TS, Bax A, Cole NB, Nussbaum RL (2005) Structure and dynamics of micelle-bound human alpha-synuclein. *J Biol Chem* 280:9595–9603.
13. Drescher M, *et al.* (2008) Antiparallel arrangement of the helices of vesicle-bound alpha-synuclein. *J Am Chem Soc* 130:7796–7797.

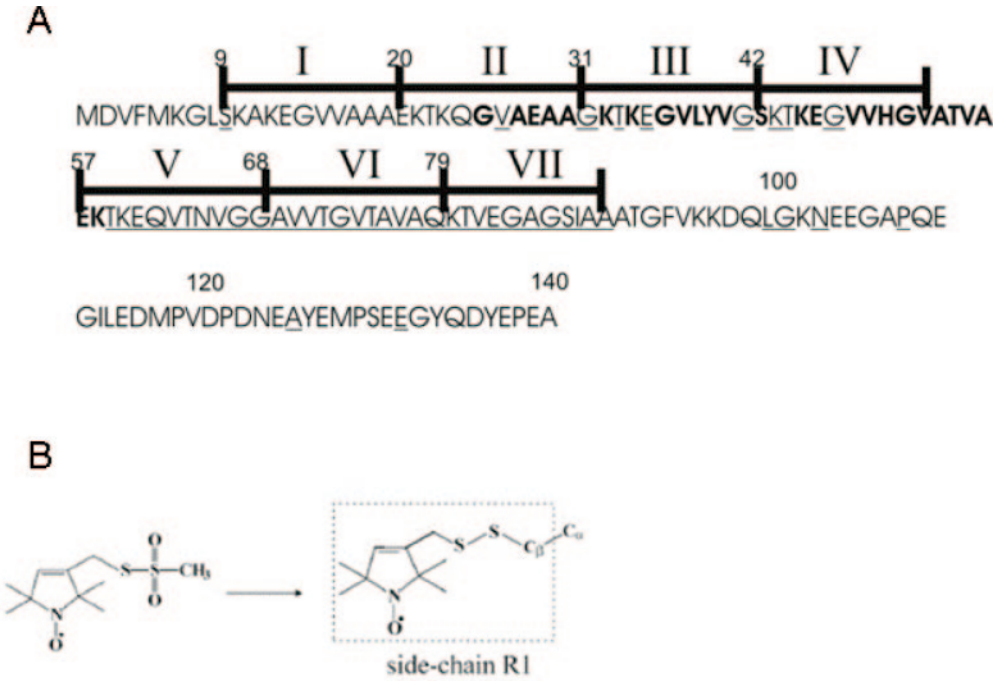

Fig. S1. (*A*) The 140-aa human α-synuclein has seven N-terminal 11-residue repeats, whose starting positions are highlighted above the vertical bars. The individual repeats are numbered in roman numerals. Letters in boldface denote sites where single substitutions to R1 were made and underlined letters denote those previously made [Jao CC, Der-Sarkissian A, Chen J, Langen R (2004) Structure of membrane-bound alpha-synuclein studied by site-directed spin labeling. *Proc Natl Acad Sci USA* 101:8331–8336]. Numbers above the sequence denote amino acid positions. In all, accessibility data for residues 25 through 90 are reported. (*B*) The reaction of the spin label [1-oxy-2,2,5,5-tetramethyl-D-pyrroline-3-methyl)methanethiosulfonate (MTSL)] with the sulfhydryl group of cysteine, resulting in the generation of the side chain R1.

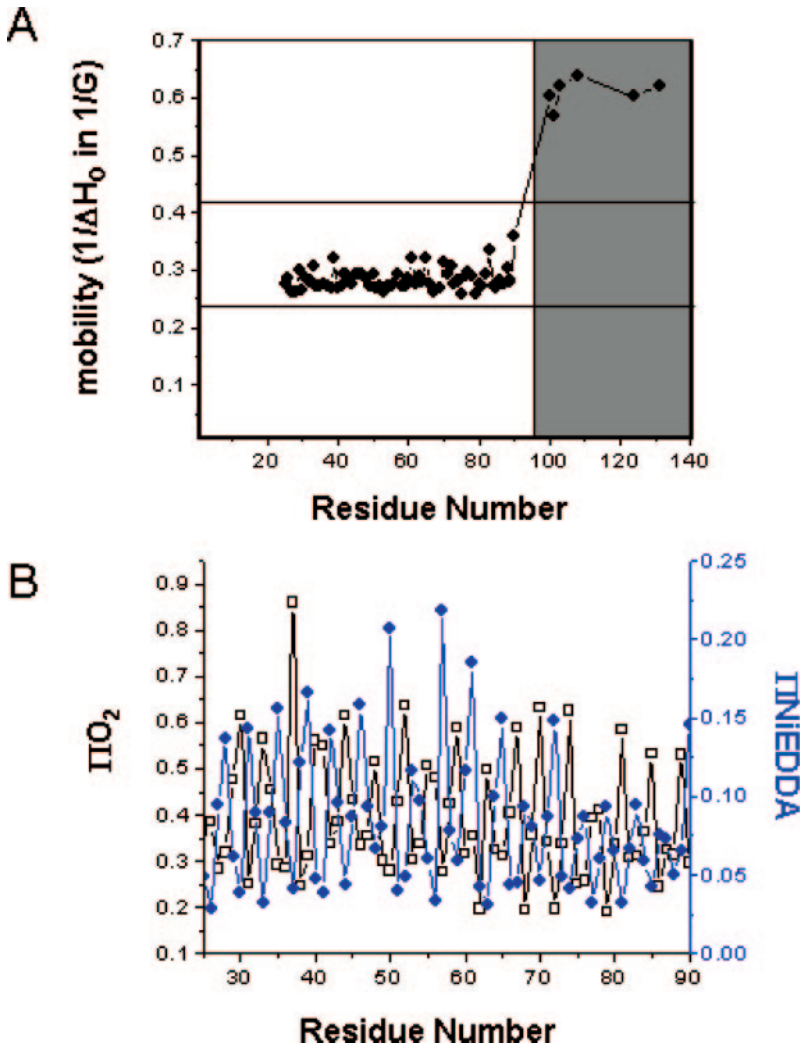

Fig. S2. (*A*) The inverse of the central line width (in 1/G) was obtained from the X-band EPR spectra of singly-labeled membrane-bound α-synuclein derivatives and is given as a function of the labeling position. The respective values obtained for N-terminal sites indicate mobilities that are typically observed for helix surface sites lacking significant tertiary or quaternary interactions. In contrast, the C-terminal sites (gray-shaded area) exhibit elevated mobility that is typically observed for disordered and unfolded regions. The horizontal lines indicate the upper and lower limits of the values typically observed for helix surface sites (1–3). *A* and *B* contain data from sites examined in the present study as well as those from our previous study (4) (see Fig. S1 for a complete listing). (*B*) Secondary structure and topology of membrane-bound, R1-labeled α-synuclein reveals an elongated helix. Nitroxide accessibility to O_2 (ΠO_2, black open squares) and NiEDDA (ΠNiEDDA, blue filled circles) are plotted as a function of residue numbers. ΠO_2 as well as ΠNiEDDA gives rise to a periodic oscillation of 3–4 residues that is characteristic of an α-helical structure. Importantly, ΠO_2 and ΠNiEDDA are out of phase, indicating an asymmetrically-solvated helix, wherein one face is exposed to the phospholipid and the other face is exposed to the solvent.

1. Mchaourab HS, Lietzow MA, Hideg K, Hubbell WL (1996) Motion of spin-labeled side chains in T4 lysozyme. Correlation with protein structure and dynamics. *Biochemistry* 35:7692–7704.
2. Isas JM, Langen R, Haigler HT, Hubbell WL (2002) Structure and dynamics of a helical hairpin and loop region in annexin 12: A site-directed spin labeling study. *Biochemistry* 41:1464–1473.
3. Margittai M, Fasshauer D, Pabst S, Jahn R, Langen R (2001) Homo- and heterooligomeric SNARE complexes studied by site-directed spin labeling. *J Biol Chem* 276:13169–13177.
4. Jao CC, Der-Sarkissian A, Chen J, Langen R (2004) Structure of membrane-bound alpha-synuclein studied by site-directed spin labeling. *Proc Natl Acad Sci USA* 101:8331–8336.

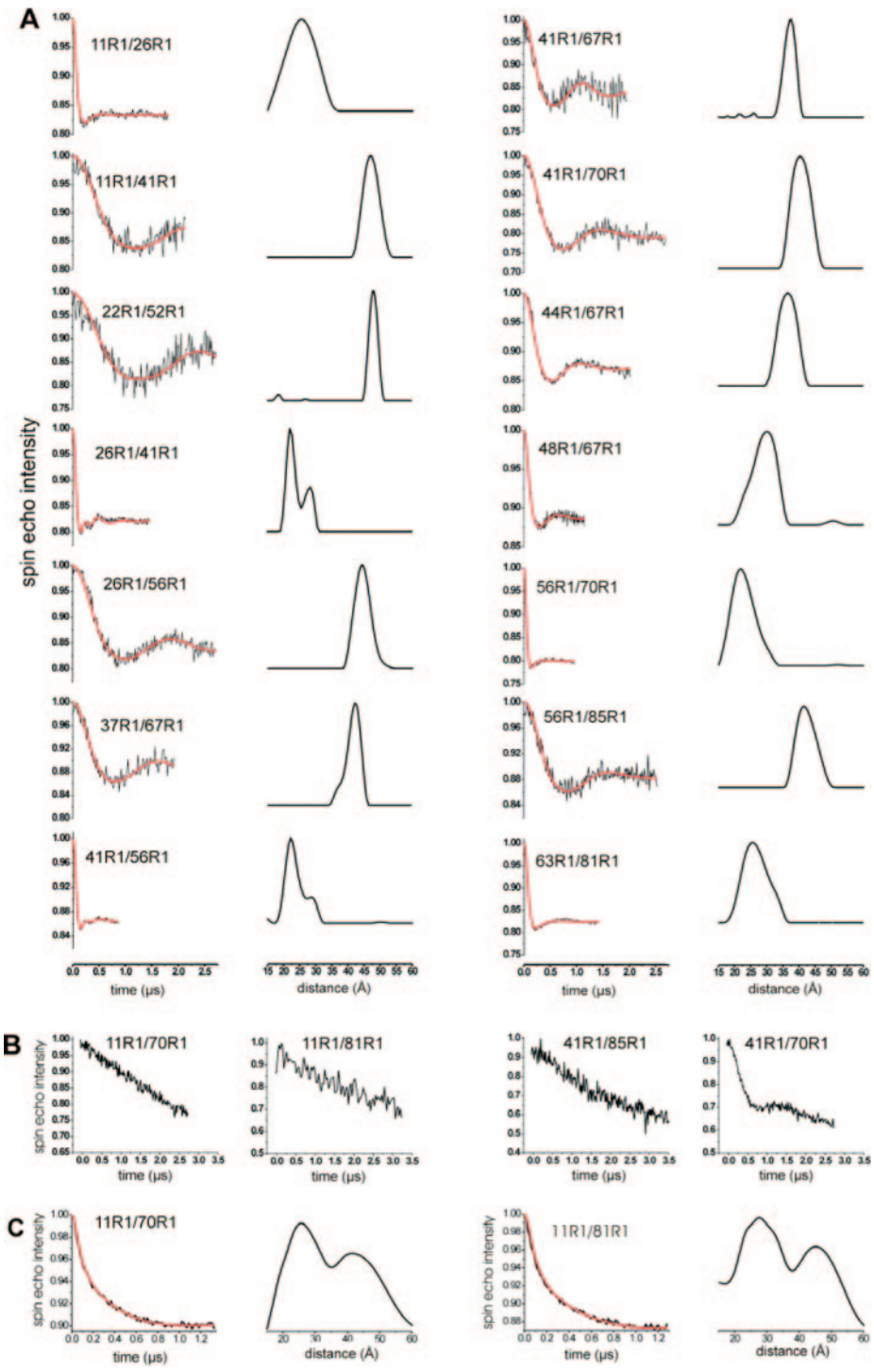

Fig. S3. Intramolecular distances from 4-pulse DEER experiments. (*A*) The *Left* panels show the dipolar evolution time for each of the indicated doubly-labeled derivatives bound to SUVs containing POPS/POPC (molar ratio of 3:7). The black traces are background-corrected experimental data and the red lines represent the results of fits using Tikhonov regularization [Jeschke G, *et al*. (2006) DeerAnalysis2006—A comprehensive software package for analyzing pulsed ELDOR data. *Appl Magn Reson* 30:473–498]. The *Right* panels show the resulting distance distributions, whose peaks are tabulated in Table 1. Gaussian fits gave rise to distance maxima that were within 0.5 Å of those shown here. Two of the double mutants containing a label at position 41 (26R1/41R1 and 41R1/56R1) show a subtle bimodal distance distribution. The minor peak, which contains about 20–30% of the signal in both cases, is shifted by approximately 5 Å compared with the main peak. The exact origin of the bimodal distance distributions is not known, but it could arise from different, well-resolved R1 rotameric states or minor heterogeneities in the backbone structure at position 41. The effect is rather subtle, however, and no bimodal distance distribution could be observed for two other double mutants containing a label at position 41 (11R1/41R1 and 41R1/70R1). Regardless, collectively all distances as well as the continuous-wave EPR data indicate an extended helical structure as the predominant form. (*B*) The distances for some double mutants were too long to determine reliably. The first three panels in *B* give the raw dipolar evolution time data for 11R1/70R1, 11R1/81R1, and 41R1/85R1, respectively. When compared to the corresponding raw data for 41R1/70R1, which did result in a clear distance, it becomes apparent that the signals for the former decay rather slowly and do not give a clear oscillation that can be fitted. This is a typical feature for long range distances and, thus, only a lower limit for the distances is given in Table 1. The estimate for the lower limit of ≈60 Å in Table 1 was estimated from the time scale of data acquisition with longer distances requiring longer time scans. According to Jeschke and Polyhach [Jeschke G, Polyhach Y (2007) Distance measurements on spin-labelled biomacromolecules by pulsed electron paramagnetic resonance. *Phys Chem Chem Phys* 9:1895–1910], the maximal distance that can clearly be resolved from DEER data obtained for 3 to 3.5 μs is on the order of 60 Å. There is a hint of an oscillation for the 41R1/85R1 derivative (corresponding to a distance of ≈60–70 Å), but a longer time scan would be required to determine the baseline unambiguously and obtain reliable distance measurements. Such longer time scans, however, gave data with poor signal to noise. (*C*) The *Left* panels shows the dipolar evolution time for the indicated α-synuclein derivatives in the presence of SDS micelles (see *SI Methods*). The black traces are the background-corrected experimental data and the red lines indicate the fits using Tikhonov regularization. The *Right* panels give the resulting distance distributions.

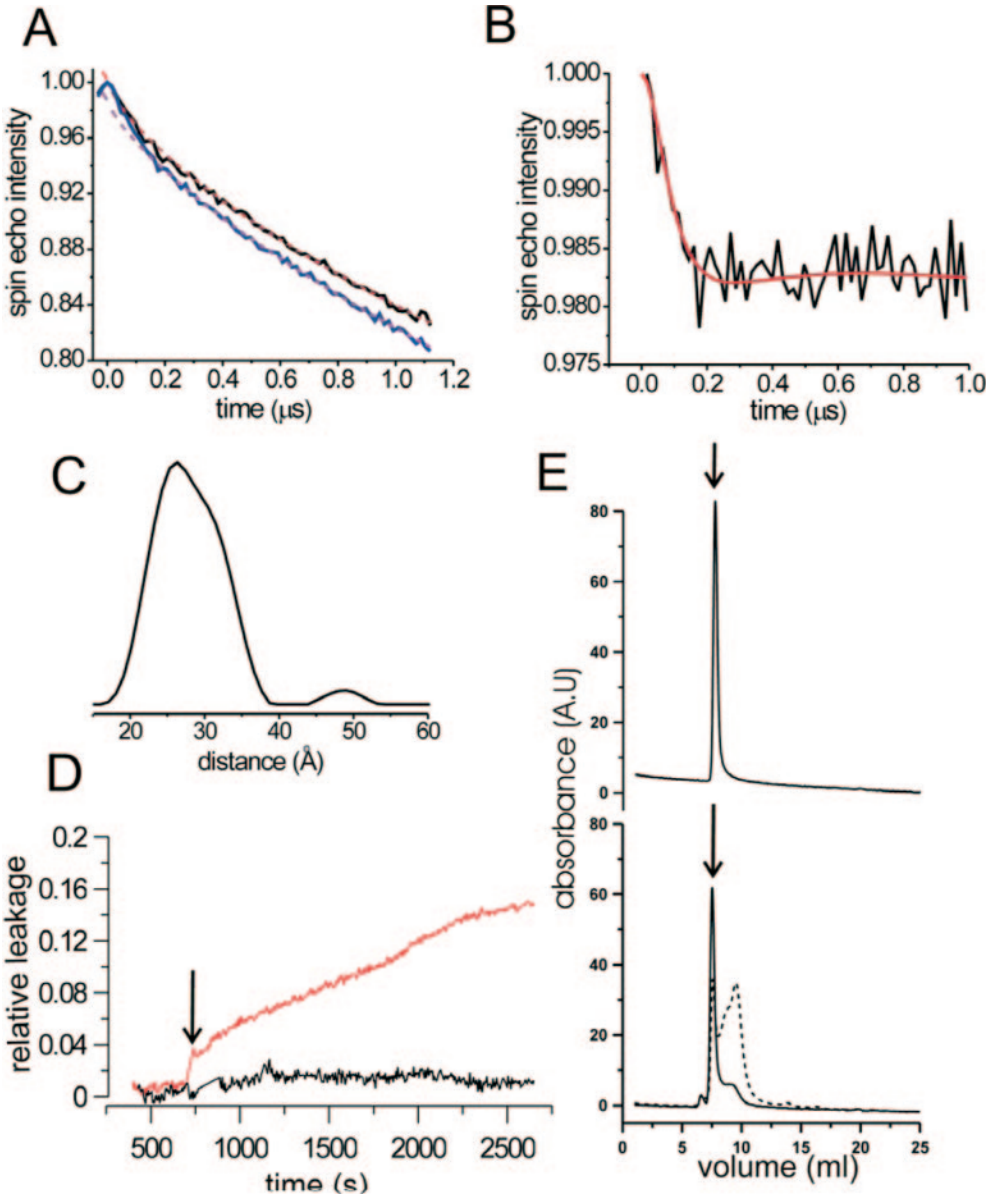

Fig. S4. α-Synuclein interaction with SUVs of different lipid compositions. (*A*) The structural features of α-synuclein bound to SUV containing 100% POPG were investigated by performing 4-pulse DEER experiments of the 11R1/70R1 derivative before (blue trace) and after purification (black trace) of the vesicle peak shown in *E*. The dipolar evolution time data after purification (black line) are difficult to distinguish from background (red dashed line) and cannot readily be fitted to obtain a distance. Thus, these data indicate a long distance and are different from those obtained for SDS micelles (Fig. S3*C*). Slight deviations from background (magenta dashed line) can be observed for the time evolution data from the unpurified sample, and the corresponding baseline-corrected time evolution data are shown as a black trace in *B*. The red line in *B* represents a fit using Tikhonov regularization and the resulting distance distribution is given in *C*. (*D*) Leakage of vesicle content was assayed by dilution of the fluorophor–quencher pair into the extravesicular space and monitored by using the fluorescence at 520 nm (see *SI Methods*). No leakage was detected for SUVs containing 100% POPG (red trace) or 3POPS/7POPC (black trace) before the addition of α-synuclein. Leakage was observed immediately after the addition of 2 μM α-synuclein to SUVs containing 100% POPG (indicated by arrow). In contrast, little or no membrane disruption was detected for the 3POPS/7POPC-containing SUVs, indicating that those SUVs remain intact upon α-synuclein binding (black). (*E*) To further investigate the vesicle perturbation observed in *A*, we performed gel filtration using Superdex 200. (*Upper*) The elution profile for 100% POPG vesicles containing 0.1% rhodamine label, which conveniently allowed for lipid detection by monitoring absorbance at 570 nm. A single peak corresponding to intact vesicles is obtained. (*Lower*) Upon addition of α-synuclein, the peak corresponding to intact vesicles remains (see arrow), but an additional lipid peak can be observed (solid line). This peak comes later and is shifted to sizes that are smaller than those of the intact vesicles. α-Synuclein was visualized by using NBD labeling at position 131, and its dilution profile was monitored at 478 nm (dashed line). While some of the protein co-eluted with the intact vesicles, the majority of the protein eluted in the second peak. From the elution profiles and the extinction coefficients for NBD and rhodamine, we were able to estimate a protein-to-lipid ratio of ≈1/50, with latter fractions having progressively more protein. These fractions, which are α-helical by circular dichroism, contain significantly more α-synuclein than is typically accommodated on SUVs consistent with the formation of protein–lipid complexes that are no longer sealed vesicular structures. As predicted from the lack of leakage in *A*, this second peak was absent when 30% POPS vesicles were used in the gel-filtration assay (data not shown).

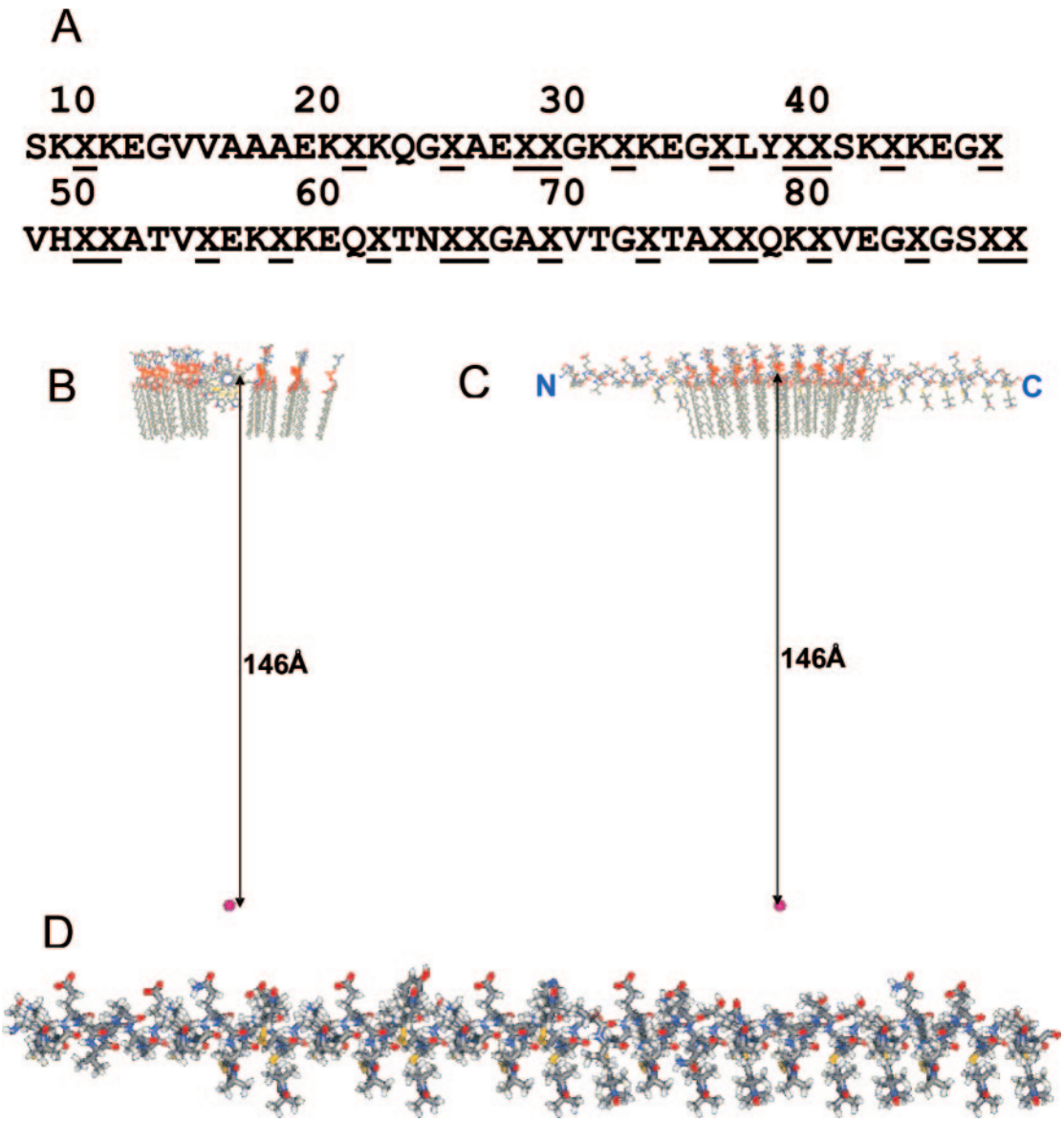

Fig. S5. Starting structure for the synuclein-(9–89) peptide with 26 labels. (*A*) The 81-aa peptide fragment (residues 9–89 of synuclein) with 26 spin labels (X) used in the SAMD simulation. (*B*) The peptide was constructed as a linear α-helix with its center positioned 146 Å from the center (pink dot) of an imaginary spherical lipid vesicle. Some lipids of the outer leaflet of the vesicle are shown to give an improved sense of the location of the peptide. The radius of the vesicle (the distance from the center of the sphere to the P atom of the phosphate group of the lipid) was 150 Å. (*C*) Rotation through 90° showing that the center of the α-helix is 146 Å from the lipid center. Amino acids in the central region of the helix were initially positioned ''below'' the phosphate head groups, whereas those at the N and C termini were ''above'' the head groups. (*D*) Close-up structure of the starting peptide, showing that the spin labels were generally oriented toward the center of the imaginary vesicle. All lipids were removed before SAMD calculations, but an ''atom'' representing the center of the sphere was used in the SAMD.

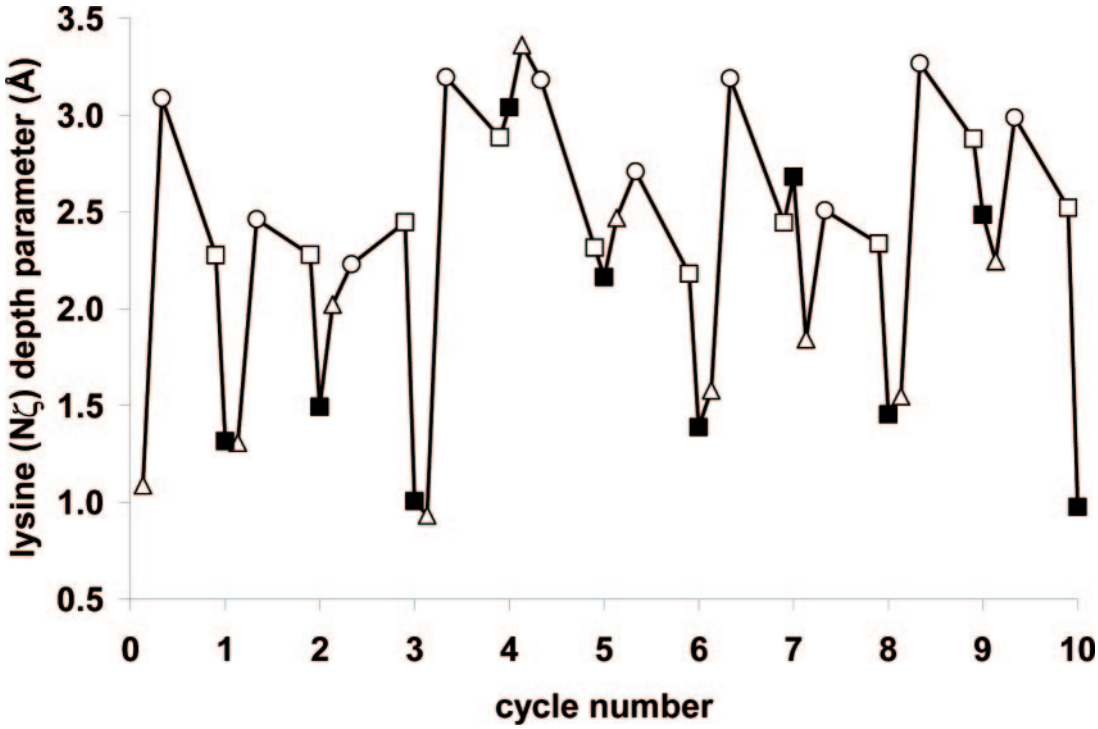

Fig. S6. Plot illustrating the behavior of seven lysine side chains (K32, K34, K43, K45, K58, K60, and K80) during the 10 production cycles of simulated annealing molecular dynamics. The depth for each lysine was calculated based on the distance from the N^{ζ} atom of each lysine to the center of the vesicle. The difference in this depth from the experimental depth was evaluated for each lysine and averaged over the 7 residues to give the ''lysine depth parameter'' for each structure in the simulated annealing calculation (150 structures per cycle, collected at steps of 0.2 ps). The plot shows this parameter at four points in each cycle reflecting averages of distances from 0 to 4 ps (initial heating from ≈0 to ≈300 K, △), 4–10 ps (rapid heating to >1,000 K, ○), 10–27 ps (slow cooling to ≈300 K, □), and 27–30 ps (cooling from ≈300 K to ≈0 K, ■).

Table S1. Label depths used in SAMD calculations

Label	Measured depth,* Å	Distance from center,† Å	Label	Measured depth,* Å	Distance from center,† Å
11	12.8	137.2	59	9.5	140.5
26	11.3	138.7	63	12.3	137.7
29	8.0	142.0	66	9.0	141.0
30	12.2	137.8	67	11.1	138.9
33	12.8	137.2	70	11.2	138.8
37	13.9	136.1	74	12.0	138.0
40	10.4	139.6	77	10.6	139.4
41	11.6	138.4	78	7.3	142.7
44	11.5	138.5	81	13.1	136.9
48	7.9	142.1	85	10.9	139.1
51	9.8	140.2	88	6.8	143.2
52	10.9	139.1	89	8.2	141.8
56	11.7	138.3			

*Depth of the label below the phosphate group of the lipid based on EPR accessibility data and depth calibration using spin-labeled lipids (see *Methods*).
†Distance from the label (assumed to be from the N atom of the nitroxide group) to the center of an imaginary lipid vesicle of diameter 300 Å. This value is calculated as 150 Å − n Å, where n is the measured depth and 150 Å is the radius.

Table S2. Restraints used in SAMD calculations

Geometry element	Structural element	Value*	$r1^{\dagger}$	$r2^{\dagger}$	$r3^{\dagger}$	$r4^{\dagger}$
Interlabel distance, Å	Label pairs in Table 1‡	Exp. *n*, Å	$n - 3$	$n - 2$	$n + 2$	$n + 3$
Label–vesicle center distance, Å	Labels in Table S1	Exp. *n*, Å	$n - 1$	$n - 0.5$	$n + 2.5$	$n + 3$
ϕ torsion angle, °	All amino acids	−57	−77	−72	−42	−37
ψ torsion angle, °	All amino acids	−47	−67	−62	−32	−27
ω torsion angle, °	All amino acids	180	177	178	182	183
Backbone H-bond distance, Å	All amino acids	2.15	1.3	1.8	2.5	3.0
H^{α}–S^{δ} distance, Å	All labels	2.8	1.8	2.3	3.3	3.8

*The value is either the experimental data or an "idealized" value for the particular geometry element.

†In AMBER8, restraints for simulated annealing are included using a modified square-well potential defined between *r*2 and *r*3, between which the variable can move freely without incurring an energy penalty. Outer limits of *r*1 and *r*4 are also defined, with force constants (*rk*2 and *rk*3) defining the energy penalty in the regions *r*1 to *r*2 and *r*3 to *r*4. The maximum values of *rk*2 and *rk*3 were set at 10.0 kcal·mol^{-1}·Å^{-1} or 10.0 kcal·mol^{-1}·degree^{-1} for all restraints.

‡Twelve label pairs for which distances were obtained, excluding 26R1/41R1 and 56R1/70R1.

Table S3. Geometry of structures obtained in SAMD calculations

Cycle	Distance 26–41,* Å	Distance 56–70,* Å	Average ϕ,† °	Average ψ,† °	SD ϕ,‡ °	SD ψ,‡ °
1	24.0	20.8	−65.0	−41.5	3.7	7.0
2	20.5	20.5	−65.0	−41.5	3.6	7.2
3	23.2	22.0	−65.4	−41.7	4.2	7.9
5	21.2	16.1	−65.3	−41.8	3.6	7.1
6	24.8	23.5	−64.9	−41.6	4.1	6.8
7	24.1	21.3	−64.3	−42.9	4.3	7.8
8	26.1	21.2	−64.7	−42.2	3.4	6.5
9	23.4	22.7	−64.2	−42.4	3.8	7.5
10	21.7	22.6	−65.4	−41.3	3.5	8.0

*Distance between the N atoms of the nitroxide in the respective labels.
†Backbone torsion angle averaged over 81 amino acids.
‡Standard deviation of the backbone torsion angle averaged over 81 amino acids.